

A Modification of Nb-Rich Portion for Refractory Nb–Ni Alloy Phase Diagram with New Peritectoid Transition



J.F. ZHAO, H.P. WANG, and B. WEI

The Nb-rich region of refractory Nb–Ni alloy phase diagram was refined by thermal analysis, long-time annealing experiments, and electron probe microanalysis (EPMA). Both metallography and EPMA results indicate that the Nb₂Ni phase is a new stable intermetallic phase with a stoichiometric composition. Thermal analyses show that the peritectoid transition of (Nb) + Nb₇Ni₆ → Nb₂Ni occurs at the temperature of 1569.7 K. In addition, the powder XRD results suggest that the equilibrium lattice constants of Nb₇Ni₆, Nb₂Ni, and (Nb) phases are $a = 4.957 \text{ \AA}/c = 27.000 \text{ \AA}$, $a = 11.594 \text{ \AA}$, and $a = 3.299 \text{ \AA}$, respectively.

<https://doi.org/10.1007/s11661-022-06906-9>

© The Minerals, Metals & Materials Society and ASM International 2022

I. INTRODUCTION

THE refractory Nb–Ni binary alloy is particularly interesting for developing the multi-component Ni-based high-temperature superalloys. Many of precipitation strengthening phases containing Nb element are present in these alloys, such as the Laves phase based on the (Ni, Fe)₂(Nb, Ti) and the γ'' phase based on the NbNi₃.^[1–5] On the other hand, this alloy system is one of the earliest binary amorphous alloy systems with the highest glass-forming ability. In the Nb–Ni binary alloy, the amorphous encountered in a wide composition range of 30–70 at.pct of Nb by mechanical alloying, and the best glass former is Nb₃₈Ni₆₂ alloy.^[6–10] To predict the phase equilibrium of multi-component superalloys based on the constituent alloy systems and investigate the crystallization kinetics of crystal phase from the amorphous alloys, the accurate phase diagram and thermodynamic properties of Nb–Ni binary system are necessary.

To establish the stable phase diagram, several researchers have investigated the phase equilibria of Nb–Ni system by experiment and thermodynamic modeling.^[11–20] Grube *et al.*^[11] first studied the liquidus and solidus of Ni-rich region of Nb–Ni binary system by thermal analysis. Subsequent researches^[12–15] showed an excellent agreement with Grube *et al.*;^[11] however, an

adopted data in Ni-rich side were provided by Duerden and Hume-Rothery.^[15] Although the solidus temperature is larger than the data of Grube *et al.*,^[11] Pogodin and Zelikman,^[12] the data of Duerden and Hume-Rothery^[15] were preferred because the solidus temperature was determined using the heating curve, avoiding the undercooling problems. Moreover, Duerden and Hume-Rothery^[15] extended the equilibrium phase diagram to the entire composition range of Nb–Ni system. Their data were consistent with other researchers,^[11–14] especially when the Nb content is less than 50 pct. For the determination of liquidus temperature in the Nb-rich region, Duerden and Hume-Rothery^[15] used the optical pyrometry method, and Wicker *et al.*^[16] employed the thermal analysis and electron microprobe analysis. The data of the former are higher about 200 °C than that provided by latter. During the process of assessing the equilibrium diagram of the Nb–Ni system, Nash and Nash^[17] chose the liquidus data of Wicker *et al.*^[16] However, according to the thermal analysis of Nb₆₀Ni₄₀ and Nb₆₅Ni₃₅ alloy, Chen *et al.*^[18] pointed out that the Nb-rich liquidus temperature provided by Duerden and Hume-Rothery^[15] is consistent with their measurement. In order to further refine the Nb–Ni equilibrium diagram, and resolve some disputes of Ni₈Nb phase and Nb-rich liquidus, Chen *et al.*^[18] measured the liquidus, solidus, and phase boundary in a wide composition range of 5–65 at.pct of Nb by thermal analysis and chemical analysis. The data of Chen *et al.*^[18] were in excellent agreement with earlier researchers,^[11–16] except for Svechnikov^[13] in some cases, which was ascribed to a calibration problem. Since Chen *et al.*^[18] used high purity pure metal, calibrated the temperatures, and determined the phase transition temperature by heating curve, their phase diagram has been accepted by other researchers.

J.F. ZHAO, H.P. WANG, and B. WEI are with the School of Physical Science and Technology, Northwestern Polytechnical University, Xi'an 710072, P.R. China. Contact e-mail: hpwang@nwpu.edu.cn

Manuscript submitted September 5, 2022; accepted November 6, 2022.

Article published online November 27, 2022

According to the equilibrium phase diagram revised by Chen *et al.*,^[18] the Nb–Ni binary system contains five solid phases: terminal solid solution (Nb) and (Ni), intermetallic compounds Nb₇Ni₆, NbNi₃ and NbNi₈. The extension solubility of each phase has been determined by several researchers using chemical analysis. However, the extension of the homogeneity range of the Nb₇Ni₆ phase at low temperatures needs additional experimental investigations, because this phase is of distinctly variable composition. Very recently, the present authors^[21] reported a new thermodynamically stable intermetallic compound Nb₂Ni with crystallographic complex face-centered cubic structure, which is generated from the peritectoid transition: (Nb) + Nb₇Ni₆ → Nb₂Ni, and the transformation temperature is 1533 K. The atomic arrangement and stability of the Nb₂Ni phase were systematically investigated employing high-resolution transmission electron microscopy analysis, theoretical density functional theory calculation, and annealing experiments. Although the composition range of Nb₂Ni phase was roughly determined as 67.39–68.38 at.pct Nb, the homogeneity range of the equilibrium Nb₂Ni phase still needs to be further refined by electron probe microanalysis (EPMA), especially in the high-temperature section.

The aim of the present work is to determine the transition temperature and the homogeneity range of Nb₂Ni phase in the Nb-rich region which has not been well established yet. To this end, four decisive alloys in the composition range of 60 to 80 at.pct Nb were selected to perform annealing experiments at a series of temperatures and times. Based on the experimental results, the Nb-rich region phase diagram of refractory Nb–Ni alloy system was established.

II. EXPERIMENTAL METHOD

The Nb–Ni master alloys were prepared from pure Nb (99.95 pct) and Ni (99.995 pct) in the arc melting furnace according to the alloy atomic compositions. Before melting, the arc melting furnace was evacuated to 3×10^{-4} Pa and then backfilled with pure argon gas to 10^5 Pa. At the same time, a titanium getter was used to prevent the oxidation of master alloys. The melting process was repeated at least three times to ensure that the sample of about 1.5 g is homogeneous. It is confirmed that the weight losses were less than the 0.1 pct in the arc melting process.

To prevent the master alloys and Ti from reacting with quartz ampoules, they were put into the alumina crucible separately. Then, both alumina crucibles were encapsulated in a quartz ampoule which was evacuated and refilled with Ar gas for 9–10 times. The final pressure backfilled Ar gas atmosphere inside the quartz ampoule was determined from the ideal gas equation and annealing temperature. The annealing experiments were performed in a high-temperature furnace at different temperatures for extended period of time: 1523 K for 100 hours, 1423 K for 200 hours, 1273 K for 500 hours, and 773 K for 700 hours, and more details are displayed in Table I. The Nb element content of

water-quenched specimens was used to determine the homogeneity range at high temperature. The equilibrium specimens were annealed at 1523 K for 100 hours and cooled down with a cooling rate of 1 K/min in the furnace.

The thermal analysis experiments were carried out with a Netzsch DSC 404C differential scanning calorimeter. The calorimeter temperature was calibrated with the melting points of purity In, Sn, Zn, Al, Ag, Au, and Ni elements. The phase transformation temperatures were determined using the equilibrium specimens with a heating and cooling rate of 5 K/min under an argon atmosphere with a flow rate of 60 mL/min. For determining the elements composition and homogeneity range of phases, EPMA was carried out on a Shimadzu EPMA-8050G, employed with wavelength dispersive spectrometer, with an accelerating voltage of 15 kV and a beam current of 20 nA. Some specimens were analyzed by energy-dispersive X-ray spectroscopy (EDS) using a Tescan Clara GMH scanning electron microscope (SEM) equipped with an AztecOne system from OXFORD. In order to determine phase constitutions and lattice parameters, the powder X-ray diffractometer (XRD) was completed on a PANanalytical X'pert MPD Pro with Cu K_α radiation, and the diffraction angle 2θ ranges from 30 to 130 deg with an increasing rate of 4 deg/min.

III. RESULTS AND DISCUSSION

A. Metallography of Heat Treatment Samples

Our previous work demonstrated that the composition of the equilibrium Nb₂Ni phase is closed to 66.67 at.pct Nb.^[21] In order to accurately determine the homogeneity range of the equilibrium Nb₂Ni phase in a wide temperature range, the annealing alloy compositions must be distributed on both sides of 66.67 at.pct Nb. As a result, four decisive alloys of Nb₆₀Ni₄₀, Nb_{66.67}Ni_{33.33}, Nb₇₀Ni₃₀, and Nb₈₀Ni₂₀ were selected to perform the annealing experiments at a series of temperatures and times, as listed in Table I. Figure 1 shows the microstructures of annealing specimens at different heat treatment conditions. The experimental results indicate the white dendrite is primary (Nb) phase, the gray matrix is peritectic Nb₇Ni₆ phase, and black region between (Nb) and Nb₇Ni₆ phases is Nb₂Ni phase. Since the Nb₂Ni phase is complex intermetallic compound, the different grain orientations will cause the difference in image contrast. To clearly distinguish the morphological characteristics of peritectoid transition, a part of Nb₂Ni phase is marked by arrows, as plotted in Figure 1. Similar morphological characteristics are also discovered in Nb₇Ni₆ grains, the matrix phase contains slatted areas that are close to the image contrast of Nb₂Ni phase, which is caused by the different grain orientations, as presented in Figures 1(b2), (c2), (d2). According to the microstructures of Nb–Ni alloys annealed at different conditions, it can be found that the size of Nb₂Ni phase in specimens annealed at 1523 K is larger than 10 μm and decreases with the

Table I. Heat Treatment Temperature and Time for Different Alloy Compositions Using Two Methods

| Heat Treatment Experiments | Temperature (K) | Time (h) | Cooling | Nb Content (at.pct) |
|----------------------------|-----------------|----------|-----------------------|---------------------|
| I | 1523 | 100 | water-quenched | 60/66.67/70/80 |
| II | 1423 | 300 | water-quenched | 60/66.67/70/80 |
| III | 1273 | 500 | water-quenched | 60/66.67/70/80 |
| IV | 773 | 700 | water-quenched | 60/66.67/70/80 |
| V | 1523 | 100 | 1 K/min (equilibrium) | 60/66.67/70/80 |

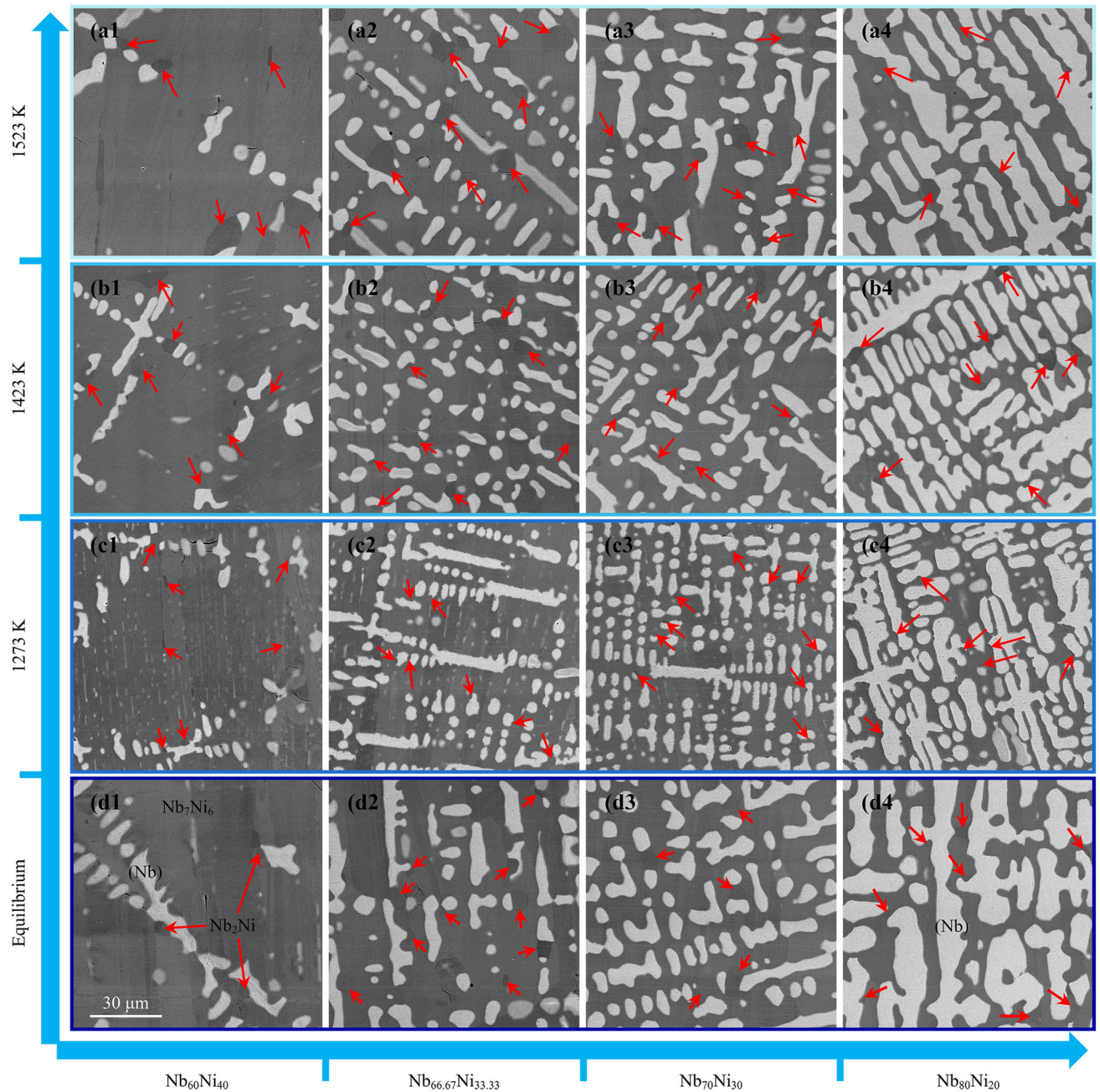


Fig. 1—Microstructures of Nb–Ni alloys annealed at different conditions: (a1 through a4) 1523 K/100 h; (b1 through b4) 1423 K/300 h; (c1 through c4) 1273 K/500 h; (d1 through d4) equilibrium (Nb_2Ni phase was marked by red arrows) (Color figure online).

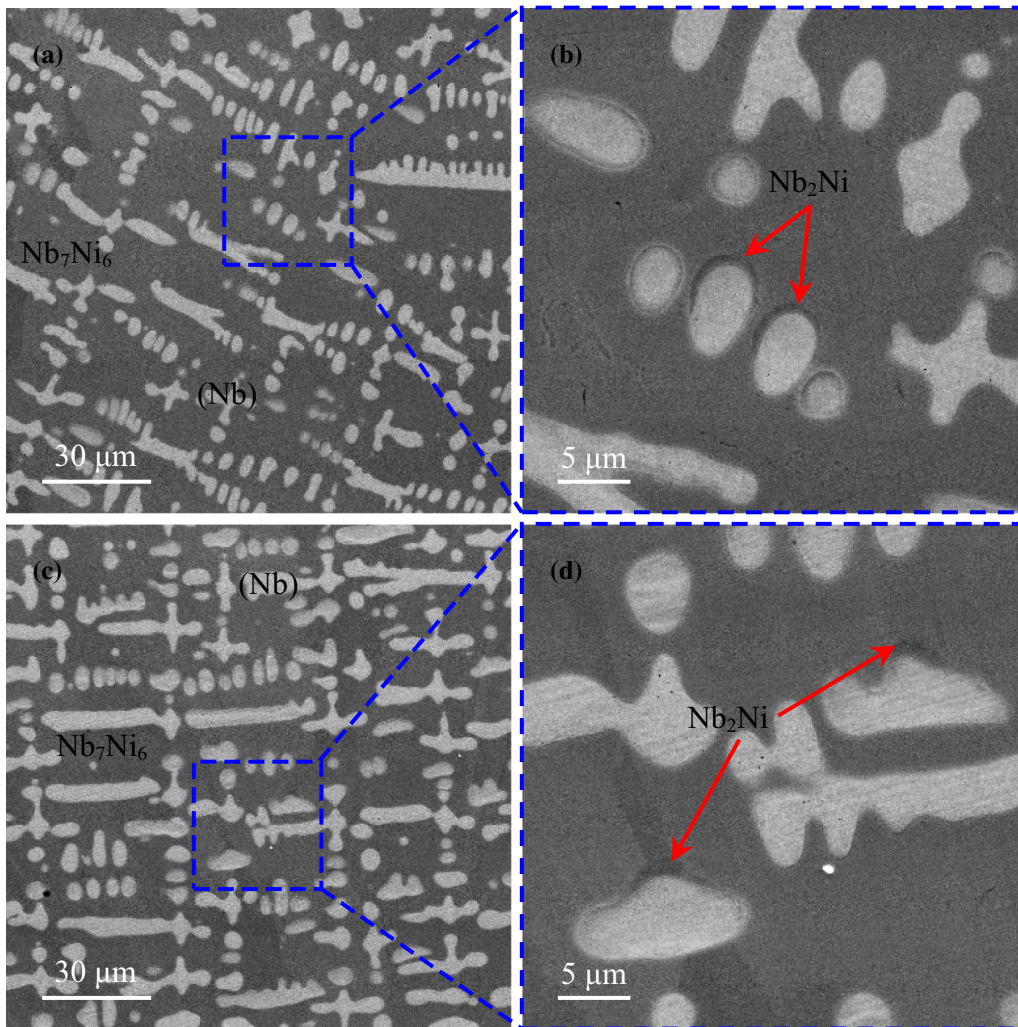


Fig. 2—Microstructures of annealing specimens at 773 K for 700 h: (a, b) $\text{Nb}_{66.67}\text{Ni}_{33.33}$ alloy; (c, d) $\text{Nb}_{70}\text{Ni}_{30}$ alloy.

reduction of the annealing temperature. Although the annealing time increases with the decrease of annealing temperature, the size of Nb_2Ni phase still reduces. Specifically, when the Nb–Ni alloys specimens were annealed at 1273 K for 500 hours, the maximum size of Nb_2Ni phase is smaller than $5\ \mu\text{m}$. The size of Nb_2Ni phase will further decrease when the specimens annealed at 773 K for 700 hours. To clearly illustrate the morphological characteristics, Figure 2 shows the microstructures of $\text{Nb}_{66.67}\text{Ni}_{33.33}$ and $\text{Nb}_{70}\text{Ni}_{30}$ alloys. According to the enlarged images Figures 2(b) and (d), it can be explicitly seen that the Nb_2Ni phase is located at the interface of primary (Nb) phase and peritectic Nb_7Ni_6 phase, which is a classical peritectoid transition morphological characteristic. Additionally, the thickness of Nb_2Ni phase along with the reaction interface is smaller than $1\ \mu\text{m}$.

B. Equilibrium Lattice Constants

To investigate the lattice constants of Nb_7Ni_6 , Nb_2Ni , and (Nb) phases with different solidification conditions, the powder XRD experiments were conducted for ingot

and equilibrium samples, and corresponding results are illustrated in Figure 3. It can be found that the positions of diffraction peaks of Nb_7Ni_6 phase within equilibrium samples are larger than that of ingot samples, on the contrary, the diffraction peaks of (Nb) phase will drift into a low angle, which indicates that the lattice constants of equilibrium Nb_7Ni_6 phase are smaller than that of ingot samples, and the lattice constant of equilibrium (Nb) phase is larger than that of ingot samples. It is worth noting that there are characteristic diffraction peaks of Nb_2Ni phase in the XRD patterns of equilibrium samples, and these characteristic diffraction peaks are marked by blue arrows, as shown in the upper right corner of Figures 3(a) through (d). However, the XRD patterns of ingot samples do not contain characteristic diffraction peaks of Nb_2Ni phase, implying that the Nb_2Ni phase almost was not generated in ingot samples. According to the XRD patterns, the lattice constants of these phases were calculated by Rietveld method and are illustrated in Table II. It can be found that the lattice constants of each phase in ingot or equilibrium samples hardly change with the alloy compositions. The lattice constants of Nb_7Ni_6 phase within equilibrium samples are significantly smaller

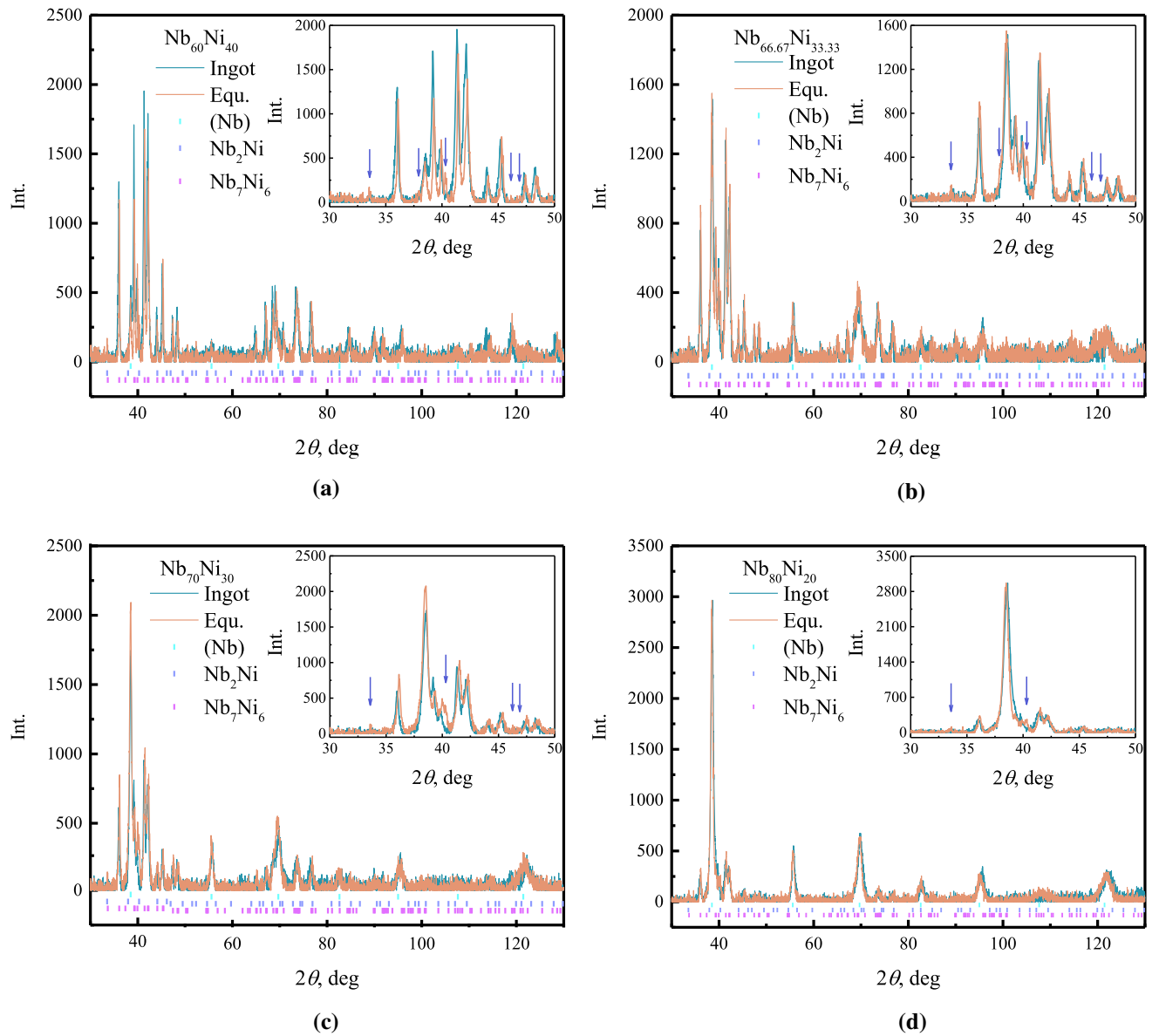


Fig. 3—Powder X-ray diffraction patterns of Nb–Ni alloys solidified at different conditions: (a) Nb₆₀Ni₄₀; (b) Nb_{66.67}Ni_{33.33}; (c) Nb₇₀Ni₃₀; (d) Nb₈₀Ni₂₀.

Table II. Lattice Constants of Nb₇Ni₆, Nb₂Ni, and (Nb) Phases Within Nb–Ni Alloys Solidified at Different Conditions

| Alloys | States | Nb ₇ Ni ₆ | | | Nb ₂ Ni | (Nb) |
|---|--------|---------------------------------|-------------|---------------------|--------------------|-------|
| | | <i>a</i> /Å | <i>c</i> /Å | <i>c</i> / <i>a</i> | | |
| Nb ₆₀ Ni ₄₀ | ingot | 4.970 | 27.042 | 5.441 | — | 3.294 |
| | equ. | 4.960 | 27.008 | 5.445 | 11.593 | 3.299 |
| Nb _{66.67} Ni _{33.33} | ingot | 4.970 | 27.049 | 5.442 | — | 3.293 |
| | equ. | 4.958 | 27.000 | 5.446 | 11.596 | 3.300 |
| Nb ₇₀ Ni ₃₀ | ingot | 4.969 | 27.036 | 5.440 | — | 3.292 |
| | equ. | 4.953 | 26.972 | 5.445 | 11.591 | 3.298 |
| Nb ₈₀ Ni ₂₀ | ingot | 4.969 | 27.075 | 5.448 | — | 3.291 |
| | equ. | 4.955 | 27.021 | 5.454 | 11.595 | 3.299 |

than that within ingot, and the lattice constants of equilibrium (Nb) phase are larger than that of ingot (Nb) phase. Owing to the fact that ingot samples solidified under a constant cooling rate, the solidification microstructures deviate from the equilibrium samples, and the solubility of each phase in ingot samples is also close to the solubility of the high temperature in the phase diagram. As we all know, the element content will influence the lattice constant. The Goldschmidt atomic radius of Ni is 1.25 Å which is smaller than 1.47 Å of Nb atom. The phase diagram of the Nb–Ni system indicates that the solubility of Ni atom within (Nb) phase reduces with the decreasing temperature and the solubility of Ni atom within Nb₇Ni₆ phase increases with decreasing

temperature. Therefore, the lattice constants of equilibrium Nb₇Ni₆ phase are smaller than that of ingot Nb₇Ni₆ phase, and the lattice constant of (Nb) phase within equilibrium samples is larger than that of (Nb) phase within ingot samples. The average lattice constants of Nb₇Ni₆ phase within ingot samples are $a = 4.970 \text{ \AA}/c = 27.051 \text{ \AA}$, which are significantly smaller than the TEM results $a = 5.042 \text{ \AA}/c = 27.437 \text{ \AA}$ of the Nb₅₄Ni₄₆ ingot sample by our previous work^[10] and the XRD result $a = 5.086 \text{ \AA}/c = 27.66 \text{ \AA}$ by Kripyakevych and Pylaeva.^[22] The average lattice constants of equilibrium Nb₇Ni₆ phase are $a = 4.957 \text{ \AA}/c = 27.000 \text{ \AA}$ that coincide with the XRD result $a = 4.959 \text{ \AA}/c = 26.999 \text{ \AA}$ of Nb₆₀Ni₄₀ alloy reported by Joubert and Feutelais.^[23] The average lattice constant of equilibrium (Nb) phase is $a = 3.299 \text{ \AA}$. As the Ni atoms with a smaller radius replace the Nb atoms on the lattice, the equilibrium lattice constant of (Nb) phase is smaller than the $a = 3.303 \text{ \AA}$ of pure Nb evaluated by Ito *et al.*^[24] The equilibrium lattice constant of Nb₂Ni phase is $a = 11.594 \text{ \AA}$, which is significantly smaller than the TEM result $a = 11.888 \text{ \AA}$; however, this value is slightly larger than the DFT result $a = 11.516 \text{ \AA}$ of our previous work about the equilibrium Nb₂Ni phase.^[21]

C. Phase Transitions and Phase Diagram

To confirm transition temperatures of the peritectic reaction $L + (\text{Nb}) \rightarrow \text{Nb}_7\text{Ni}_6$ and the peritectoid reaction $(\text{Nb}) + \text{Nb}_7\text{Ni}_6 \rightarrow \text{Nb}_2\text{Ni}$, equilibrium samples were conducted for thermal analysis with two heating-cooling cycles. Transition temperatures were obtained using heating curves, and Figure 4 displays the second heating curves of equilibrium samples and corresponding transition temperatures. DSC measurement results show that the peritectic reaction temperature is 1577.8 K, which is in good agreement with the

temperature of $1575 \pm 2 \text{ K}$ measured by Chen *et al.*^[18] This value is higher than 1563 K reported by Wicker *et al.*^[16] and 1568 K given by Duerden and Hume-Rothery,^[15] but smaller than 1593 K measured by Svechnikov *et al.*^[13] The peritectoid reaction temperature is confirmed as 1569.7 K, which is significantly larger than 1533 K of our previous work about Nb₅₄Ni₄₆ alloy.^[21] It is worth mentioning that the peritectic temperature based on the heating curve of Nb₅₄Ni₄₆ alloy is also smaller than that of this work. The peritectic reaction generally could not completely proceed, and therefore, in addition to the peritectic Nb₇Ni₆ phase, the final solidification microstructure of Nb₅₄Ni₄₆ alloy contains the primary (Nb) phase and eutectic of Nb₇Ni₆ and NbNi₃ phase. During the heating process, the eutectic phase will melt at 1453 K, and the liquid phase may reduce the energy barriers of subsequent peritectoid and peritectic reactions, which makes the reaction temperatures significantly smaller than the actual values. Therefore, the peritectoid reaction temperature should be confirmed as 1569.7 K.

To determine the homogeneity range of Nb₂Ni phase and refine phase boundaries of (Nb) and Nb₇Ni₆ phase, the Nb contents of phases in heat treatment specimens under different conditions were measured by EPMA and EDS, and corresponding results are illustrated in Figure 5 and Table III. Figure 5 visually displays the elements distribution of equilibrium Nb_{66.67}Ni_{33.33} specimen. Comparing with the Nb EDS mapping, the difference of each phases can be easily distinguished from the Ni element EDS mapping, especially the Nb₂Ni phase. Additionally, the overlay EDS mapping of Nb and Ni can totally reveal the distribution of Nb₂Ni phase contained those regions which cannot be readily found in Figure 5(a), as marked by cerulean blue circle in Figure 5(d). As shown in Figures 1(c1) and (c4), when the heat temperature is lower than 1273 K, the sizes of Nb₂Ni phase are smaller than 5 μm. As a result, the EPMA data of Nb₂Ni phase are replaced by EDS data. While the specimens annealed at 773 K for 700 hours, the Nb contents of (Nb) phase and Nb₇Ni₆ phase still deviate significantly from that in the equilibrium specimens. Therefore, these data were not used to determine the solubility range. The EPMA results demonstrate that the Nb content of Nb₇Ni₆ phase decreases with the reduction of temperature, and on the contrary, the Nb content of (Nb) increases with the decreasing temperature. Although the Nb content of Nb₂Ni phase in Nb₆₀Ni₄₀ alloy is slightly lower than that in Nb₈₀Ni₂₀ alloy, this difference value can be neglected when the error of measurement is considered. Therefore, the Nb₂Ni phase has a constant composition point, which is different from the Nb₇Ni₆ phase with distinctly variable composition.

Based on the EPMA data, transition temperatures of present work, and the literature data, the refined phase diagram of Nb-rich region of Nb–Ni system was established, as shown in Figure 6. As the peritectoid transition temperature is close to the peritectic reaction temperature, the peritectoid transition line is marked by red to distinguish the peritectoid transition line and peritectic reaction line, and an enlarged image is also displayed in Figure 6(b). According to Figure 6(a), it can be found that the Nb contents of Nb₇Ni₆ phase are consistent with the EPMA data measured by Chen

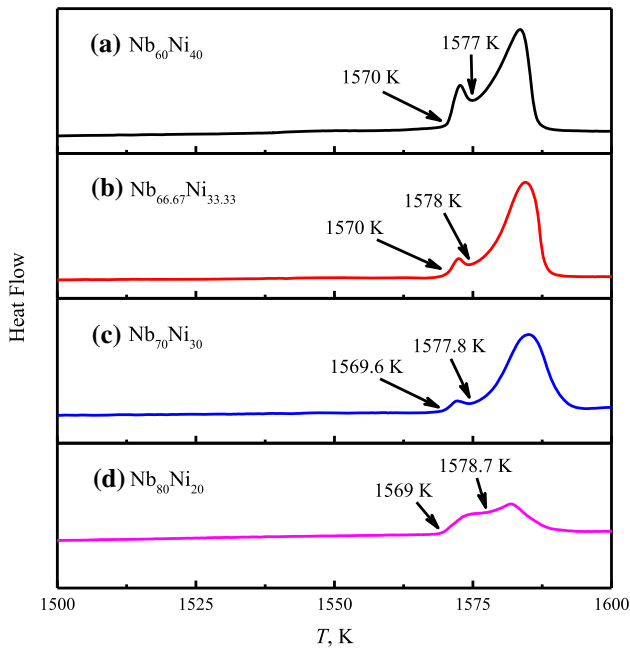


Fig. 4—Thermal analysis curves of Nb–Ni alloys: (a) Nb₆₀Ni₄₀ alloy; (b) Nb_{66.67}Ni_{33.33} alloy; (c) Nb₇₀Ni₃₀ alloy; (d) Nb₈₀Ni₂₀ alloy.

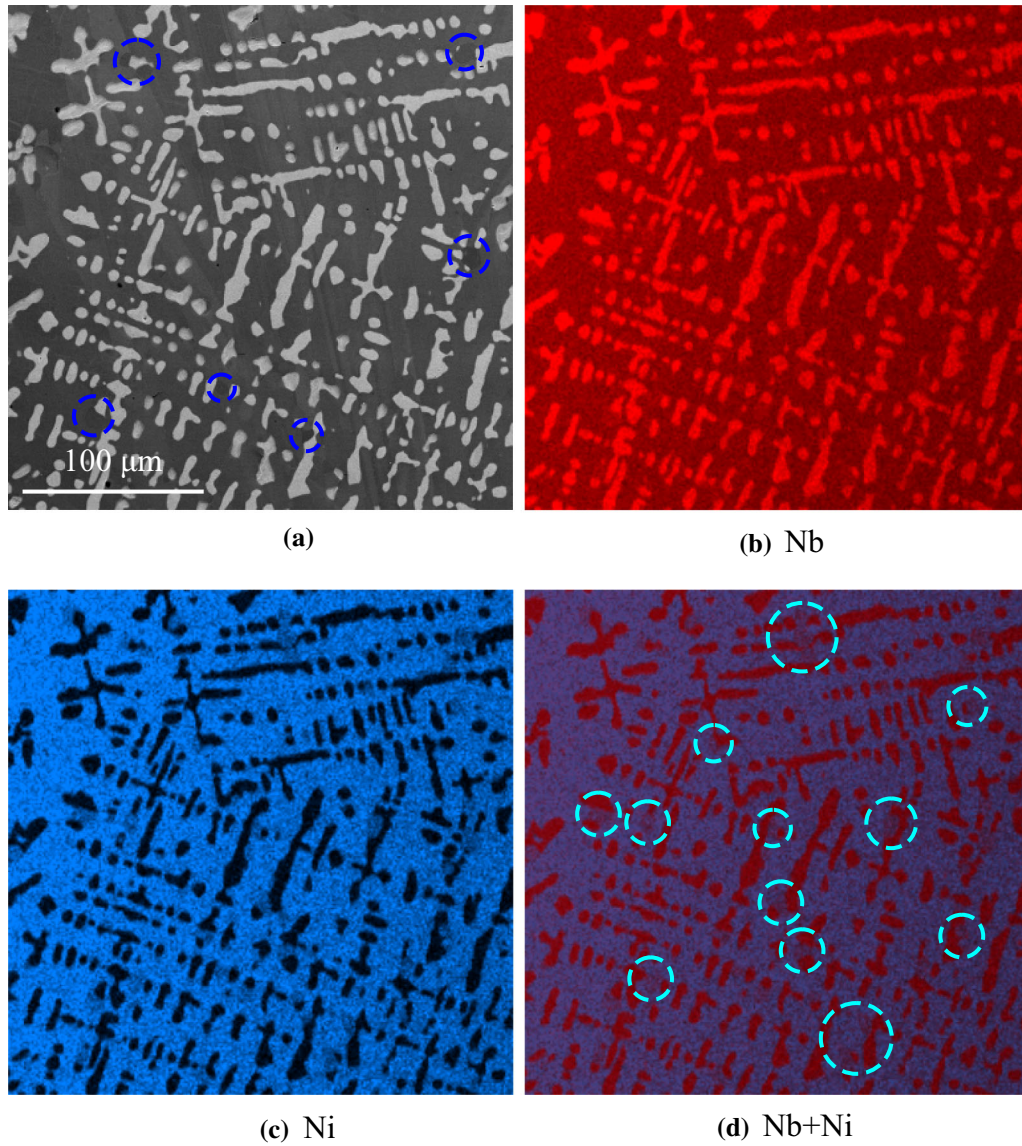


Fig. 5—EDS mapping of equilibrium $\text{Nb}_{66.67}\text{Ni}_{33.33}$ specimen: (a) microstructures; (b) Nb EDS mapping image; (c) Ni EDS mapping image; (d) Nb + Ni EDS mapping image.

Table III. Nb Content (Atomic Percentage) of Three Phases Within Nb–Ni Alloys Annealed at Different Conditions Obtained by EPMA and EDS (Unit of Heat Treatment is K/h)

| Alloys | Phase | 1523 K/100 h | 1423 K/300 h | 1273 K/500 h | 773 K/700 h | Equilibrium |
|--|--------------------------|------------------|------------------|--------------------|------------------|------------------|
| $\text{Nb}_{60}\text{Ni}_{40}$ | (Nb) | 96.54 ± 0.42 | 96.65 ± 0.22 | 96.94 ± 0.30 | 95.44 ± 0.34 | 96.68 ± 0.20 |
| | Nb_2Ni | 66.06 ± 0.37 | 66.11 ± 0.49 | $64.57 \pm 1.11^*$ | — | 66.09 ± 0.32 |
| | Nb_7Ni_6 | 56.16 ± 0.20 | 56.14 ± 0.46 | 55.70 ± 0.33 | 57.36 ± 0.51 | 56.31 ± 0.25 |
| $\text{Nb}_{66.67}\text{Ni}_{33.33}^*$ | (Nb) | 95.58 ± 0.45 | 96.19 ± 0.35 | 96.20 ± 0.33 | 94.40 ± 0.55 | 96.23 ± 0.57 |
| | Nb_2Ni | 65.16 ± 0.61 | 65.23 ± 0.33 | 65.19 ± 1.58 | — | 64.91 ± 0.59 |
| | Nb_7Ni_6 | 55.55 ± 0.57 | 55.39 ± 0.28 | 54.44 ± 0.60 | 55.96 ± 0.50 | 54.76 ± 0.40 |
| $\text{Nb}_{70}\text{Ni}_{30}^*$ | (Nb) | 96.11 ± 0.65 | 96.16 ± 0.54 | 96.23 ± 0.45 | 94.84 ± 0.35 | 94.71 ± 0.82 |
| | Nb_2Ni | 65.21 ± 0.33 | 65.09 ± 0.39 | 64.36 ± 1.88 | — | 63.76 ± 0.35 |
| | Nb_7Ni_6 | 55.63 ± 0.37 | 55.39 ± 0.67 | 54.75 ± 0.61 | 56.40 ± 0.52 | 53.93 ± 0.59 |
| $\text{Nb}_{80}\text{Ni}_{20}$ | (Nb) | 97.51 ± 0.39 | 97.64 ± 0.54 | 97.44 ± 0.34 | 96.54 ± 0.23 | 97.91 ± 0.42 |
| | Nb_2Ni | 66.46 ± 0.32 | 66.19 ± 2.81 | $65.80 \pm 1.66^*$ | — | 66.59 ± 0.26 |
| | Nb_7Ni_6 | 56.35 ± 0.25 | 56.36 ± 0.37 | 56.27 ± 0.13 | 57.77 ± 0.35 | 56.08 ± 0.42 |

*Data are obtained by EDS.

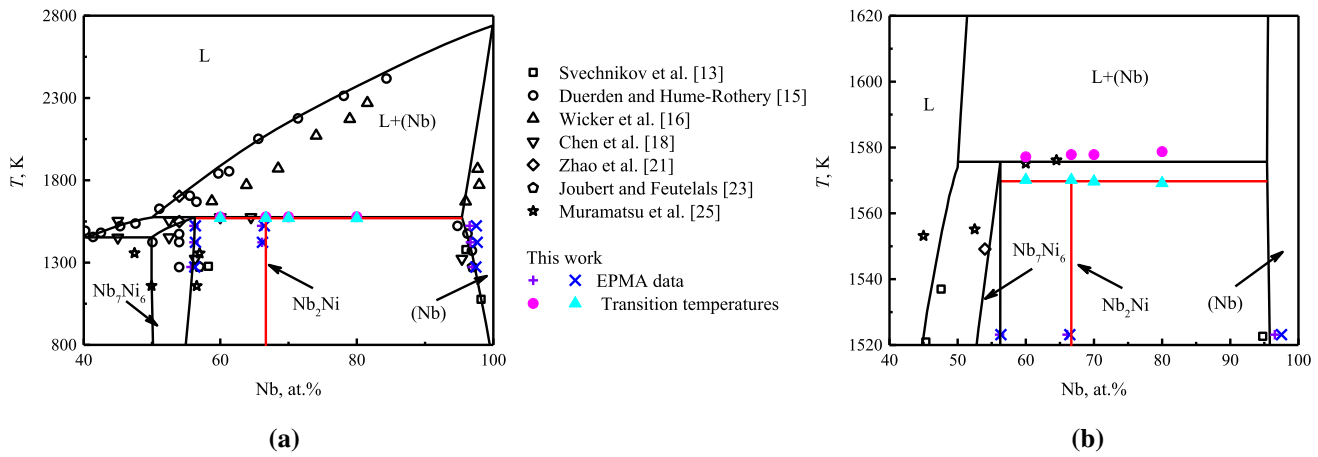


Fig. 6—The refined phase diagram of Nb-rich region of Nb–Ni system (a) and enlarged image (b).

et al.^[18] Joubert and Feutelals^[23], and Muramatsu *et al.*^[25] Duerden and Hume-Rothery^[15] reported that the maximum Nb content of Nb_7Ni_6 phase is 53.89 at.pct, which is obviously less than the measurement value of other researchers.^[13,18,25] Therefore, their data about the Nb content of Nb_7Ni_6 phase were not considered when the boundary line of Nb_7Ni_6 phase was determined. Although the Nb content of (Nb) phase at 1523 K is larger than the data obtained by Duerden and Hume-Rothery,^[15] the data at other temperatures are in excellent agreement with the value reported by Svechnikov *et al.*,^[13] Duerden and Hume-Rothery^[15], and Joubert and Feutelals.^[23] The EPMA data of Nb_2Ni phase at different temperatures visually indicate that the Nb_2Ni phase is a definite composition in the Nb–Ni phase diagram. As a result, the composition range of Nb_2Ni phase in phase diagram was represented by a line at the 66.67 at.pct Nb, as shown in Figure 6.

In summary, the Nb-rich region of refractory Nb–Ni alloy phase diagram was refined combining annealing and quenching techniques and thermal analysis. More importantly, the part related to the new peritectoid transition of Nb_2Ni phase is added to the refined phase diagram for the first time.

IV. CONCLUSIONS

The four representation Nb–Ni alloys with special compositions of $\text{Nb}_{60}\text{Ni}_{40}$, $\text{Nb}_{66.67}\text{Ni}_{33.33}$, $\text{Nb}_{70}\text{Ni}_{30}$, and $\text{Nb}_{80}\text{Ni}_{20}$ were selected to perform the annealing experiments at a series of temperature and time. Both EPMA and DSC techniques were used to determine the phase compositions and transition temperatures. The long-time annealing experiments confirm that the Nb_2Ni phase is a stable phase in refractory Nb–Ni binary system. The EPMA results indicate that the compositions of Nb_7Ni_6 and (Nb) phases agree well with the previous data reported by other researchers. In particular, the EPMA data secure that the Nb_2Ni phase has a stoichiometric composition within the Nb–Ni alloy phase diagram. Additionally, the peritectoid transition temperature of

(Nb) + Nb_7Ni_6 → Nb_2Ni is determined as 1569.7 K by DSC experiments. Based on the present work and the literature data, the refined phase diagram of Nb-rich region for refractory Nb–Ni alloy system is proposed. Especially, the temperature of peritectoid transition and the composition range are supplemented as a modification. Finally, the powder XRD results indicate that the average lattice constants of equilibrium Nb_7Ni_6 , Nb_2Ni , and (Nb) phases are $a = 4.957 \text{ \AA}$ / $c = 27.000 \text{ \AA}$, $a = 11.594 \text{ \AA}$, and $a = 3.299 \text{ \AA}$, respectively.

ACKNOWLEDGMENTS

This work was supported by the National Natural Science Foundation of China (Grant Nos. 52088101 and 51734008) and the Space Utilization System of China Manned Space Engineering (Grant No. KJZ-YY-NCL02). The authors are deeply grateful to Miss. H. M. Chen, Mr. N. S. Hou, W. B. Liu, and D. D. Zuo for their help with the experiments and valuable discussion.

CONFLICT OF INTEREST

On behalf of all authors, the corresponding author states that there is no conflict of interest.

REFERENCES

1. W.L. Wang, C.Y. Zhu, J. Zeng, C. Lu, H.R. Qian, H. Xu, and P.S. Lyu: *Metall. Mater. Trans. A*, 2020, vol. 51, pp. 2306–17.
2. F. Saint-Antonin, W. Lefebvre, and I. Blum: *Crystals*, 2019, vol. 9, p. 345.
3. B. Shassere, D. Greeley, A. Okello, M. Kirka, P. Nandwana, and R. Dehoff: *Metall. Mater. Trans. A*, 2018, vol. 49, pp. 5107–17.
4. E. Chlebus, K. Gruber, B. Kuźnicka, J. Kurzac, and T. Kurzynowski: *Mater. Sci. Eng. A*, 2015, vol. 639, pp. 647–55.
5. L. Ling, Y.F. Han, W. Zhou, H.Y. Gao, D. Shu, J. Wang, M.D. Kang, and B.D. Sun: *Metall. Mater. Trans. A*, 2015, vol. 46, pp. 354–61.
6. S.R. Nagel, J. Vassiliou, P.M. Horn, and B.C. Giessen: *Phys. Rev. B*, 1978, vol. 17, pp. 462–67.

7. S. Basak, R. Clarke, and S.R. Nagel: *Phys. Rev. B*, 1979, vol. 20, pp. 4278–86.
8. D. Holland-Moritz, F. Yang, J. Gegner, T. Hansen, M.D. Ruiz-Martin, and A. Meyer: *J. Appl. Phys.*, 2014, vol. 115, p. 203509.
9. Y. Zhang, R. Ashcraft, M.I. Mendeleev, C.Z. Wang, and K.F. Kelton: *J. Chem. Phys.*, 2016, vol. 145, p. 204505.
10. J.F. Zhao, M.X. Li, H.P. Wang, and B. Wei: *Acta Mater.*, 2022, vol. 237, p. 118127.
11. G. Grube, O. Kubaschewski, and K. Zwiauer: *Z. Elektrochem.*, 1939, vol. 45, pp. 881–84.
12. S.A. Pogodin and A.N. Zelikman: *Comptes Rendus (Doklady) de L'Académie Des Sciences de L'URSS*, 1941, vol. 31, pp. 895–97.
13. V.N. Svechnikov, V.M. Pan, and V.G. Korobeinikova: *Sb. Nauchn. Rab. Inst. Metallofiz., Akad. Nauk Ukr. SSR*, 1964, vol. 19, p. 196.
14. R.S. Mints, G.F. Belyaeva, and Yu.S. Malkov: *Acad. Sci. USSR Chem. Sect. Proc.*, 1962, vol. 143, pp. 281–84.
15. I.J. Duerden and W. Hume-Rothery: *J. Less Common. Met.*, 1966, vol. 11, pp. 381–87.
16. A. Wicker, C. Allibert, J. Oriole, E. Bonnier, and C.R. Acad: *Sci. C*, 1970, vol. 271, pp. 273–75.
17. P. Nash and A. Nash: *Bull. Alloy Phase Diagrams*, 1986, vol. 7, pp. 124–30.
18. H.L. Chen, H. Du Yong, H. Xu, Y. Liu, and J.C. Schuster: *J. Mater. Sci.*, 2005, vol. 40, pp. 6019–22.
19. H. Okamoto: *J. Phase Equilib. Diffus.*, 2008, vol. 29, pp. 210–10.
20. A. Bolcavage and U.R. Kattner: *J. Phase Equilib.*, 1996, vol. 17, pp. 92–100.
21. J.F. Zhao, H.P. Wang, and B. Wei: *J. Mater. Sci. Technol.*, 2022, vol. 100, pp. 246–53.
22. P.I. Kripyakevich and E.N. Pylaeva: *Sov. Phys. Crystallogr.*, 1967, vol. 12, pp. 294–96.
23. J.M. Joubert and Y. Feutelais: *Calphad*, 2002, vol. 26, pp. 427–38.
24. M. Ito, H. Muta, M. Uno, and S. Yamanaka: *J. Alloys Compd.*, 2006, vol. 425, pp. 164–68.
25. Y. Muramatsu, F. Roux, and A. Vignes: *Trans. Jpn. Inst. Met.*, 1975, vol. 16, pp. 61–72.

Publisher's Note Springer Nature remains neutral with regard to jurisdictional claims in published maps and institutional affiliations.

Springer Nature or its licensor (e.g. a society or other partner) holds exclusive rights to this article under a publishing agreement with the author(s) or other rightsholder(s); author self-archiving of the accepted manuscript version of this article is solely governed by the terms of such publishing agreement and applicable law.